Article

Synthesis and Structural Characterization of Layered Ni$^{+1/+2}$ Oxides Obtained by Topotactic Oxygen Release on Nd$_{2-x}$Sr$_x$NiO$_{4-\delta}$ Single Crystals

Chavana Hareesh [1] , Monica Ceretti [1,*] , Philippe Papet [1], Alexeï Bosak [2], Martin Meven [3] and Werner Paulus [1,*]

1 ICGM, Univ Montpellier, CNRS, ENSCM, 34000 Montpellier, France; hareesh.chavana@umontpellier.fr (C.H.); philippe.papet@umontpellier.fr (P.P.)
2 European Synchrotron Radiation Facility, 71 Avenue des Martyrs, 38000 Grenoble, France; alexei.bossak@esrf.fr
3 Institute of Crystallography, RWTH Aachen University and Jülich Centre for Neutron Science (JCNS) at Heinz Maier-Leibnitz Zentrum (MLZ), 85748 Garching, Germany; martin.meven@frm2.tum.de
* Correspondence: monica.ceretti@umontpellier.fr (M.C.); werner.paulus@umontpellier.fr (W.P.)

Abstract: Layered nickelate oxides containing Ni^{1+}/Ni^{2+} are isoelectronic to Cu^{2+}/Cu^{3+} compounds and of present interest with respect to recent findings of superconductivity in a series of different compositions. It is thereby questionable why superconductivity is still rare to find in nickelates, compared to the much larger amount of superconducting cuprates. Anisotropic d_{z^2} vs. $d_{x^2-y^2}$ orbital occupation as well as interface-induced superconductivity are two of the main advanced arguments. We are here interested in investigating the feasibility of synthesizing layered nickelate-type oxides, where the Ni^{1+}/Ni^{2+} ratio can be tuned by oxygen and/or cation doping. Our strategy is to synthesize Sr-doped n = 1 Ruddlesden–Popper type Nd$_{2-x}$Sr$_x$NiO$_{4+\delta}$ single crystals, which are then reduced by H$_2$ gas, forming Nd$_{2-x}$Sr$_x$NiO$_{4-\delta}$ via a topotactic oxygen release at moderate temperatures. We report here on structural studies carried out on single crystals by laboratory and synchrotron diffraction using pixel detectors. We evidence the general possibility to obtain reduced single crystals despite their increased orthorhombicity. This must be regarded as a milestone to obtain single crystalline nickelate oxides, which further on contain charge-ordering of Ni^{1+}/Ni^{2+}, opening the access towards anisotropic properties.

Keywords: non-stoichiometric transition metal oxides; superconducting Ni^{1+}/Ni^{2+} nickelates; layered nickelates; charge order; single crystal growth; topotactic oxygen release

1. Introduction

Recent findings of superconductivity in Nd$_{0.8}$Sr$_{0.2}$NiO$_2$ thin films at Tc~15 K renewed the interest in nickelates for high-T$_c$ superconductivity research which is still essentially dominated by copper oxides [1]. The underlying concept is related to the isoelectronic configuration of Ni^{1+}/Ni^{2+}, compared to Cu^{2+}/Cu^{3+}, i.e., a seemingly critical valence state of the transition metal is $3d^9 - 3d^8$ [2–4]. A stimulating debate resulted in understanding the mechanism of the unconventional superconductivity in nickelates in comparison to the iso-structural and/or iso-electronic copper-based analogues. In particular, the pairing symmetry of the superconducting order parameter in nickelate superconductors is still a controversial and open question [5–7]. Theoretical calculations have supported the idea that nickelates have a similar gap symmetry to cuprates, with a dominant ($d_{x^2-y^2}$)-wave pairing, despite its multiorbital nature [1,5–9]. Alongside this theory, other propositions have been put forward, such as a d_{x-y}-wave gap or a two-gap model $d_{z^2} - \text{wave} + d_{x^2-y^2} - \text{wave}$ [10–12] or a transition between a gapped $(d + is) - \text{wave}$ to a nodal d-wave pairing state [13] for neodymium-based nickelates. First-principles density functional theory calculations also showed the role of the $4f$ magnetism [14]. In addition,

experimental spectroscopic studies on nickelate thin films have shown a mixture of d-wave and s-wave signals at different locations of the film surface, suggesting the formation of nonstoichiometric or secondary phases, thus complicating the determination of the true coupling symmetry of the superconducting gap [15]. Nickel is right next to copper in the periodic table, and it is long known to form compounds with similar structural configurations as high Tc cuprates. Hole doped superconducting cuprates show a $Cu^{2+/3+}$ mixed valence state, i.e., a $3d^9 - 3d^8$ configuration, which is considered to be a crucial parameter for high-T_C superconductivity [16]. Its nickel analogue containing $Ni^{1+/2+}$, and thus with an identical electronic configuration, is therefore also supposed to be a promising candidate for superconductivity.

The appearance of superconductivity in $Nd_{0.8}Sr_{0.2}NiO_2$ thin films was therefore an important landmark intensifying research activity to synthesize new layered $Ni^{1+/2+}$ containing oxides. However, the stabilization of Ni^{1+} is not that common but favored in higher-order Ruddlesden–Popper (RP)-type oxides with the general formula of $A_{n+1}B_nO_{3n+1}$, which, e.g., for $n = 3$ in case of $Pr_4Ni_3O_{10}$, only contains Ni^{2+}. This phase can, however, be reduced in a topotactic reaction under mild conditions (under H_2 at 360 °C) towards $Pr_4Ni_3O_8$, with an average valence state of $Ni^{1.33+}$. The Jahn–Teller distortion in nickelates is generally much less pronounced and a better understanding of their respective electronic structure thus becomes crucial in defining the extent of hybridization of nickel d-orbitals.

Similar to the cuprates, the $Ni^{1+/2+}$ mixed valence state appears to be critical for superconductivity in infinite layered compounds [17]. This is further reinforced by the experimentally evidenced superconductivity in undoped $Nd_6Ni_5O_{12}$ thin films with an average valence state of $Ni^{1.2+}$ [18]. $Nd_6Ni_5O_{12}$ has been obtained by a low-T topotactic reduction via the CaH_2 method, leading to a mixed valence state of the nickel atoms of Ni^{1+}/Ni^{2+}. The resulting layered structure is considered to be a T′ structural type similar to the electron-doped $Nd_{2-x}Ce_xCuO_4$ superconductor [19]. However, unlike cuprates, superconductivity in nickelates was primarily seen only in thin-film samples, until the recent findings on $La_3Ni_2O_7$ single crystals showing superconductivity at Tc $\approx$ 80 K under high pressures exceeding 14 GPa [20]. This bulk-type superconductivity puts into question the idea that superconductivity in nickelates is induced by substrate/interface-induced effects, thereby emphasizing the importance of having single crystalline nickelate samples for understanding the origins of superconductivity.

The non-stoichiometric RP phases with $n = 1$, e.g., La_2CuO_4 or $(Pr/Nd)_2NiO_4$, present a special case, as they can easily uptake oxygen to form $R_2BO_{4+\delta}$ [21–23], and for which its ability to release oxygen is much less studied. Their structure consists of alternating perovskite and rock-salt layers along the stacking axis, as shown in Figure 1a.

Some of these RP oxides have been shown to release oxygen, either by being reduced in H_2 atmosphere or by the CaH_2 method. Cuprates like La_2CuO_4 and Nd_2CuO_4 have been topotactically reduced to form an oxygen vacancy-ordered framework $R_2CuO_{3.5}$, containing CuO_2 dumbbells with all copper atoms being formally monovalent Cu^{1+} only [24,25]. We were therefore interested in exploring to what extent this type of reduction reaction can be transferred to RP nickelates and how oxygen vacancy ordering together with the nickel valence state can be tuned by partially substituting the trivalent rare-earth atoms by bivalent alkaline earth atoms, such as Sr. The feasibility to reduce RP frameworks with H_2 gas has been shown for polycrystalline $Nd_{2-x}Sr_xNiO_{4-\delta}$, where Ni^{1+}/Ni^{2+} valence states can indeed be formed [26,27].

The appearance or not of superconductivity in nickelates is presently discussed in terms of the d_{z^2} vs. $d_{x^2-y^2}$ orbital occupation as well as their degree of hybridization with oxygen orbitals. As an example, the double occupation of the d_{z^2} orbital in Jahn–Teller distorted La_2CuO_4, with an increased apical Cu—O_{ap} bond length, coupled to a large p-d hybridization ($d_{x^2-y^2}$), is seen as an essential trademark to mediate high-temperature superconductivity upon La substitution by Sr or O doping [16]. The Jahn–Teller distortion in nickelates is much less pronounced, and a better understanding of their respective

electronic structures thus becomes crucial in defining the extent of hybridization of nickel *d*-orbitals.
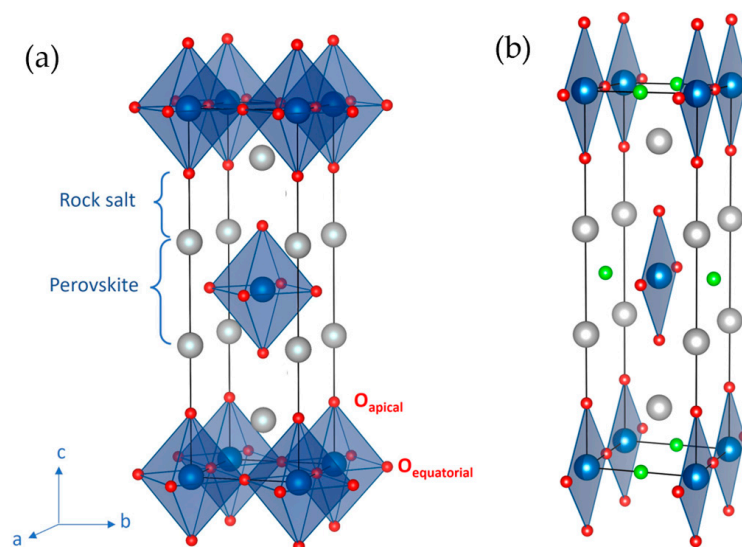
Figure 1. (**a**) Crystal structure of Ruddlesden–Popper phase $n = 1$ (R_2BO_4, where R is a rare earth and B a transition metal) in the tetragonal symmetry *I4/mmm* with alternating perovskite and rock salt layers. Rare earth atoms are represented by silver spheres, transition metal atoms by blue spheres and oxygen atoms are the red ones. (**b**) Taking out half of the equatorial oxygen atoms results in the formation of the so-called S-phase, with *Immm* symmetry. The green spheres represent the former equatorial oxygen positions that can be occupied in the case of intermediate stoichiometries.

However, it is difficult to experimentally access the orbital occupations on polycrystalline samples by spectroscopic methods. This problem can be overcome by resonant inelastic X-ray scattering (RIXS) studied on oriented single crystals (bulk/thin-film), i.e., parallel and perpendicular to the c-axis. Beside the synthetic aspects, our motivation concerns further on the feasibility of Ni^{1+}/Ni^{2+} single crystal growth. Given the straightforwardness to easily reduce polycrystalline $R_{2-x}Sr_xNiO_4$ at the higher Sr content (x > 0.3), we consequently explored the feasibility to reduce $Nd_{1.3}Sr_{0.7}NiO_{4+\delta}$ single crystals. The strategy here is to first synthesize $Nd_{1.3}Sr_{0.7}NiO_{4+\delta}$ single crystals, which are then reduced in H_2/N_2 gas mixtures at moderate temperatures towards $Nd_{2-x}Sr_xNiO_{4-\delta}$. Given that the final stoichiometry is similar to the cuprates reported above, the availability of $Nd_{2-x}Sr_xNiO_{3.5}$ type crystals would open up a panoply of studies, i.e., detailed structural features as oxygen vacancy ordering, as well as their anisotropic electronic properties.

We report below on the synthesis conditions and structural characterization of the H_2-reduced $Nd_{1.3}Sr_{0.7}NiO_{4-\delta}$ single crystals and polycrystalline powder, with mixed $Ni^{1+/2+}$ valence state, using laboratory and synchrotron single-crystal and powder X-ray diffraction techniques.

2. Materials and Methods

Synthesis and single crystal growth. Polycrystalline $Nd_{1.3}Sr_{0.7}NiO_{4+d}$ was synthesized by classical solid-state reactions at high temperature, starting from the precursor oxides. Stoichiometric amounts of Nd_2O_3, $SrCO_3$ and NiO powders (99.99% purity, Alfa Aesar, Kandel, Germany) were thoroughly ground and calcinated for 12 h at 900 °C in air. The obtained powders were then ground again and heated at 1250 °C for 24 h.

$Nd_{1.3}Sr_{0.7}NiO_{4+\delta}$ single-crystal growth was performed by using a two-mirror optical floating zone furnace as described elsewhere [28]. Seed and feed rods for crystal growth were obtained by hydrostatic pressing of the as synthesized $Nd_{1.3}Sr_{0.7}NiO_{4+\delta}$ powders at 10 bars in a cylindrical latex tube of 8 mm in diameter and 150 mm in length. To compensate for steady evaporation of NiO during the crystal growth, a 2% molar NiO excess was added

to the stoichiometric starting material. Very dense polycrystalline rods for single crystal were obtained by subsequent sintering at 1250 °C for 18 h. The crystal growth was carried out by the travelling floating zone (TFZ) method, using a two-mirror optical floating zone furnace (NEC SC2, Japan) equipped with two 500 W halogen lamps. The growth was carried out in oxygen flux with a speed rate of 3.3 mm/h with the feed and seed rods counter rotating at 30 rpm.

Micron-sized $Nd_{1.3}Sr_{0.7}NiO_{4+\delta}$ single crystals and polycrystalline samples were reduced in a 5% H_2/N_2 gas flow at 560 °C, as decomposition into the binary oxides started to set in above 650 °C.

X-ray diffraction. Phase purity of the grown crystals was checked by laboratory X-ray powder diffraction on a D8 Discover diffractometer (Bruker, Karlsruhe, Germany) equipped with a Johansson monochromator for $CuK_{\alpha1}$ radiation and a fast detector with high energy resolution (LynxEye XE-T). Powder diffraction patterns were analyzed using the FullProf suite [29] and the crystal structure is visualized using the VESTA freeware (ver. 3.5.8) [30]. Single crystal X-ray diffraction (SXRD) studies were carried out using a STADIVARI (MoK_{α} source, Xenocs Microfocus tube) diffractometer (STOE, Darmstadt, Germany) equipped with a DECTRIS 200 K Pilatus pixel-detector. In addition, synchrotron X-ray single crystal diffraction was carried out on the beamline ID28 at the European Synchrotron Facility (ESRF, Grenoble, France) ($\lambda = 0.6968$ Å), equipped with a 1 M Pilatus detector. Single-crystal data analysis was performed using the SNBL Tool Box [31], the CrysAlis blue (Rigaku-Oxford Diffraction) and an in-house developed software, with ALBULA (DECTRIS) for the visualization, as well as the X-Area software package (version 1.86, STOE, Darmstadt).

Electron microscopy. The crystal quality and elemental composition were checked by scanning electron microscopy (SEM) analysis using a JEOL JSM 6400 microscope (JEOL Ltd., Tokyo, Japan), equipped with an OXFORD INCA EDS instrument for atomic recognition via X-ray fluorescence spectroscopy. SEM/EDS analyses were performed on a cross section (6 mm in diameter) of the grown crystal after an accurate surface polishing and cleaning.

Thermogravimetric studies. To determine the overall oxygen stoichiometry, thermogravimetric (TGA) measurements were carried out using a NETZSCH thermo-balance (NETZSCH, Germany) applying a 5% H_2/N_2 gas mixture for reduction with a heating rate of 5 °C/min. Measurements were performed on ground single crystals.

## 3. Results and Discussion

3.1. Crystal Growth and Characterization

Figure 2 shows the obtained $Nd_{1.3}Sr_{0.7}NiO_{4+\delta}$ single crystal, 6 mm in diameter and 110 mm in length. Phase purity was checked by X-ray powder diffraction on a small section of the as-grown single crystal that was crushed into fine powder. From the corresponding XRD pattern, as shown in Figure 3a, the as-grown single crystal is single-phase without any impurities.

Figure 2. As-grown $Nd_{1.3}Sr_{0.7}NiO_{4+\delta}$ single crystal as obtained by floating zone method by using a mirror furnace (NEC-SC2).

| Element	Atomic (%)	Stoichiometric ratio
Ni	19.40	1
Sr	14.00	0.72(2)
Nd	24.90	1.28(3)
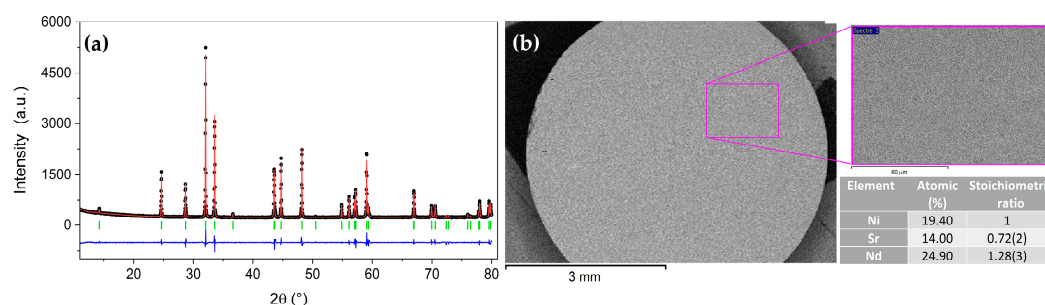
Figure 3. (**a**) Observed, calculated and difference XRD (Bruker D8 Advance, $CuK_{\alpha 1}$) patterns of the as-grown crushed $Nd_{1.3}Sr_{0.7}NiO_{4+\delta'}$ crystal indexed in *I4/mmm* space group, as obtained in profile matching mode. Dot black points are the experimental data, red line is the calculated pattern and the blue curve is the difference one. Vertical bars are related to the calculated Bragg reflection positions; (**b**) SEM images (at different scales) of the crystal cross section, showing the absence of cracks or intergrowth phases. In the insert table: summary of the elemental composition derived from by EDX and reflecting, within the experimental incertitude, the nominal composition of the as-grown $Nd_{1.3}Sr_{0.7}NiO_{4+\delta}$ single crystal (oxygen, being a light element, is difficult to quantify by EDX due to the limited sensitivity).

The pattern profile refinement carried out in the profile matching mode through the Fullprof software (5.10, version January 2023) against the *I4/mmm* space group gives the following lattice parameters: $a = b = 3.7755(3)$ Å and $c = 12.4548(1)$ Å. The chemical composition and homogeneity of the crystals were verified by SEM coupled with the EDX analysis on a section cut from the as-grown crystal. It was found to be free of cracks or inclusions of secondary phases (Figure 3b). The atomic percentages of nickel, strontium and neodymium are constant over the whole cross section, in agreement with the nominal Nd:Sr:Ni stoichiometry 1.3:0.7:1 (inset of Figure 3b).

3.2. Reduction

Polycrystalline $Nd_{1.3}Sr_{0.7}NiO_{4+\delta}$ obtained from a crushed single crystal was reduced in a 5% H_2/N_2 gas flow. The reduction curve is depicted in Figure 4, where the weight change is reported as a function of the temperature. The total weight loss amounts to almost 6%: a first oxygen loss is observed above 400 °C, while a second and larger loss starts at around 720 °C, corresponding to the decomposition into $(1 - x/2)Nd_2O_3$, $(x)SrO$ and Ni, as checked by XRD. It thus results that the oxygen stoichiometry of the starting as-grown single crystal is 4.00(2), and there is the formation of the oxygen deficient phase $Nd_{1.3}Sr_{0.7}NiO_{3.54(2)}$ at 560 °C, with an average Ni oxidation state corresponding to $Ni^{1.7+}$.

The important oxygen loss is accompanied by a change in the symmetry towards orthorhombic. After the reduction, the compound is single phase and with the profile matching refinement of laboratory X ray powder diffraction, data could be indexed in the orthorhombic *Immm* space group with lattice parameters $a = 3.6163(4)$ Å, $b = 3.8205(6)$ Å and $c = 12.6505(6)$ Å (see Figure 5). The initial fit of the X-ray data is rather poor ($\chi^2 \cong 12$) as some Bragg reflections (especially those where the a-axis is involved) show significant asymmetries and anisotropic broadening which are difficult to model. The refinement improves by the introduction of anisotropic strains using the spherical harmonics model in the fit ($\chi^2 \cong 5$), as implemented in the FullProf suite. Indeed, lattice microstrains could be present due to fluctuations in the cell parameters if the reduction reaction is not homogeneous or to antiphase/twin boundaries originating from the tetragonal-to-orthorhombic transition, as will be discussed in detail in the following section.
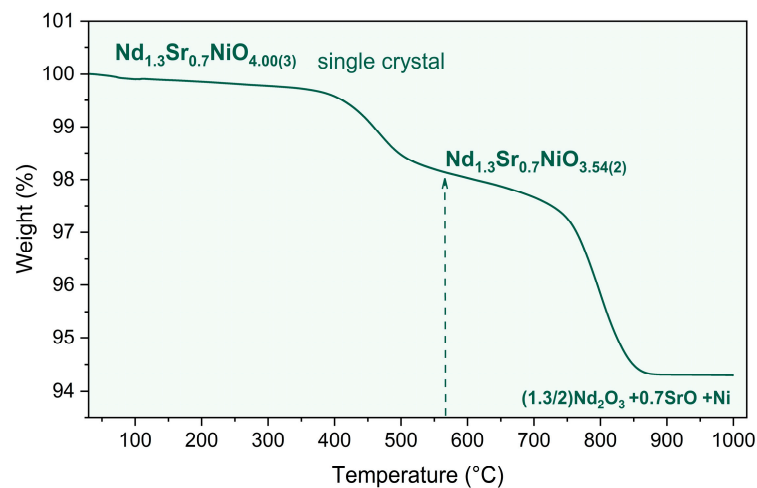
Figure 4. TGA weight loss curve obtained in 5%H_2/N_2 atmosphere with a heating rate of 5 K/min of the ground $Nd_{1.3}Sr_{0.7}NiO_{4+\delta}$ single crystal. The weight loss starting above 400 °C yields an oxygen stoichiometry corresponding to $Nd_{1.3}Sr_{0.7}NiO_{3.54(2)}$ at 560 °C.
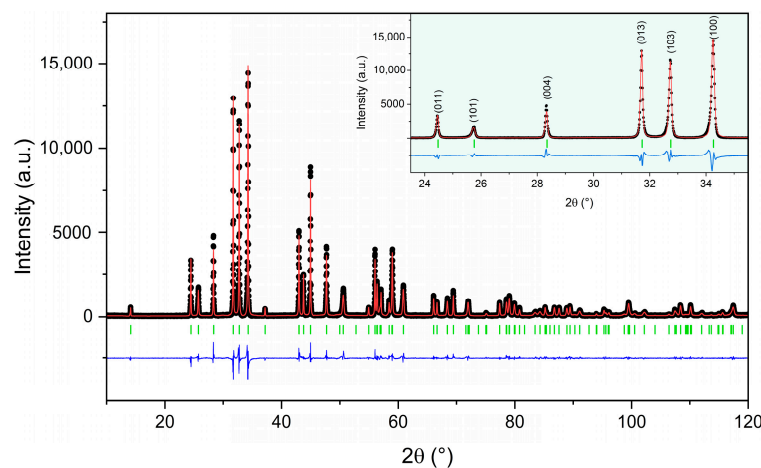

Figure 5. X-ray diffraction pattern of the reduced crushed single crystal, showing the new phase $Nd_{1.3}Sr_{0.7}NiO_{3.54(2)}$ with *Immm* symmetry (refinement in profile matching mode). Data were collected on the Brucker D8 Discover X-ray diffractometer with $CuK_{\alpha1}$. The experimental data are represented by the black dots, while the calculated pattern is indicated by the continuous red line. The blue continuous line is the difference between the experimental and calculated intensities while the short green vertical bars indicate the Bragg peak positions.

The pretty different lattices parameters after reduction imply important changes in the a/b-axes, yielding an elevated orthorhombicity (orthorhombic strain $r = (a - b)/(a + b) = 2.7\%$). From the increase in the *c*-axis, from 12.4548(1) Å of the starting phase to 12.6505(6) Å of the reduced one, it becomes evident that the O-vacancies are essentially introduced in the equatorial sites. Releasing half of the equatorial oxygen atoms in an ordered way would result in the formation of the so-called S-phase (see Figure 1b).

3.3. Single Crystal X-ray Diffraction

Figure 6a,b show the reconstructed (*hk0*) layers obtained on the single-crystal STOE STADIVARI diffractometer for the as-grown and reduced phase, respectively. The non-split single-crystal reflections of the starting crystal confirm the tetragonal symmetry, while the reflection splitting for the reduced orthorhombic phase is related to the formation of twin domains.
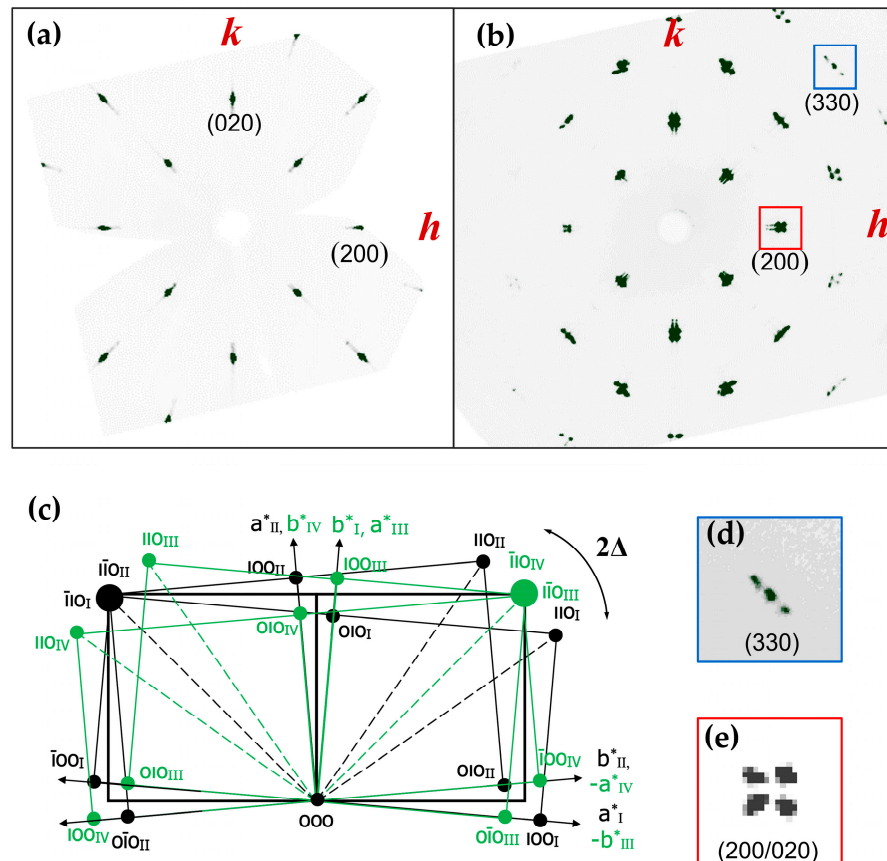
Figure 6. (**a**,**b**) (*hk0*) reconstructed diffraction planes obtained from STOE STADIVARI diffractometer for the as-grown single crystals of $Nd_{1.3}Sr_{0.7}NiO_4$ and for the $Nd_{1.3}Sr_{0.7}NiO_{3.54}$ reduced single crystal, respectively. (**c**) Schematic representation of splitting in the (*h00*), (*0k0*) and (*hk0*) reflections, expected from the tetragonal to the orthorhombic phase transition, implying the formation of four twin individuals. For clarity, each twin pair is assigned with either black or green color. (**d**,**e**) Zoom on the (*330*) and (*200/020*) Bragg reflections, clearly showing the characteristic splitting for a two-times twinned crystal, i.e., the formation of 4 orthorhombic twin individuals.

The symmetry reduction from tetragonal to orthorhombic leads to the loss of the diagonal mirror planes along [110]/[−110], becoming the common planes of the formed twin individuals (see Figure 6c). It leads to the typical splitting of (*h00*) reflections Δ, which is quantified by $\Delta = \tan^{-1}\left(\frac{a}{b}\right) - \tan^{-1}\left(\frac{b}{a}\right)$. Δ becomes twice this value for (*hh0*) reflections along [110]. It implies that a maximum of four orthorhombic twin individuals can be achieved. The respective volume fractions can be quantified by analyzing the outer "satellites" of the respective (*hh0*) and (*−hh0*) reflections. Typical values found for the reflection splitting Δ in RP phases, related to the tetragonal/orthorhombic phase transitions, are generally below Δ ≈ 1°; as an example, the stoichiometric Nd_2NiO_4 shows a domain separation with Δ = 0.89° [16]. Given the important difference of the *a/b* lattice parameters in $Nd_{1.3}Sr_{0.7}NiO_{3.54}$, the domain separation is expected to achieve almost four times this value, i.e., a Δ corresponding to 3.72°. Maintaining a faultless single-crystal characteristic during the reduction reaction thus presents an important obstacle, as the related strain increase is expected to destroy its pristine crystallinity.

The inspection of the reconstructed diffraction planes given in Figure 6 clearly indicates that, despite the elevated orthorhombicity, all diffraction peaks still remain sharp. The systematic presence of four contributions for (*h00*) reflections (Figure 6e), thereby indicates the formation of four twin individuals, presenting an equal volume fraction of (1/4). This is in agreement with a micro-twinning of the orthorhombic domains, as any unequal volume fraction distribution would rather indicate the formation of large, i.e., individual, domains.

A micro twinning is also in favor of minimizing the stress between individual domains. A complete transformation towards the reduced orthorhombic phase is indicated by the entire absence of the former, tetragonal (*h00*)-reflections, which are supposed to appear in the center of the four orthorhombic (*h00/0h0*) reflections, thus indicating a complete reduction reaction.

The angular separation of the twin domains in $Nd_{1.3}Sr_{0.7}NiO_{3.54}$ is determined to correspond to $\Delta = 3.2°$ (Figure 7b). The reflection splitting measured is 0.5° lower compared to what is expected from the orthorhombic lattice parameters obtained for polycrystalline $Nd_{1.3}Sr_{0.7}NiO_{3.54}$. This might be related to reduced reaction kinetics when compared to the powder samples having a much lower grain size. Another reason might be a different microstructure for sintered ceramics and crystallites obtained by recrystallization from the melt.
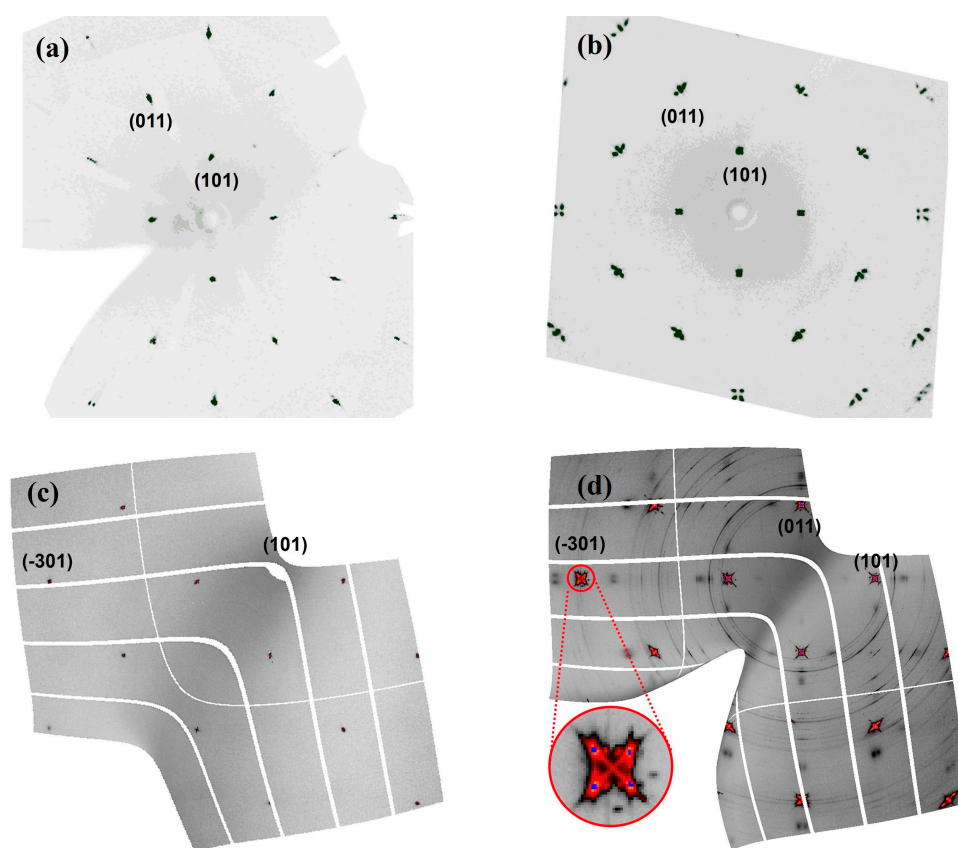
Figure 7. Reconstructed (*hk1*)-planes of the as-grown (Figure 7a,c) and reduced (Figure 7b,d) $Nd_{1.3}Sr_{0.7}NiO_{3.54}$ crystals investigated on a STOE STADIVARI diffractometer (**a,b**) and on the beamline ID28 at the ESRF (**c,d**). The high brilliance for the synchrotron study allows us to see the partial decomposition of the crystal into a randomly oriented polycrystalline fraction, together with slightly broadened reflections which appear on top of the main reflections, suggesting a Ni^{1+}/Ni^{2+} charge ordering centered on [010] with a modulation vector of $Q_n = \pm 0.4\ b^*$ applied for the 4 twin domains (*n*) as further outlined in Figure 8. The reduced binary oxides, i.e., Nd_2O_3, SrO as well as NiO, are simulated and shown in Figure A1. Diffuse scattering is observed between domains with a common twin plane, i.e., respective couples of (*hkl/khl*) reflections, as shown in the inset in Figure 7d for the (*−301/0-31*) couples, related to the formation of domain boundaries.
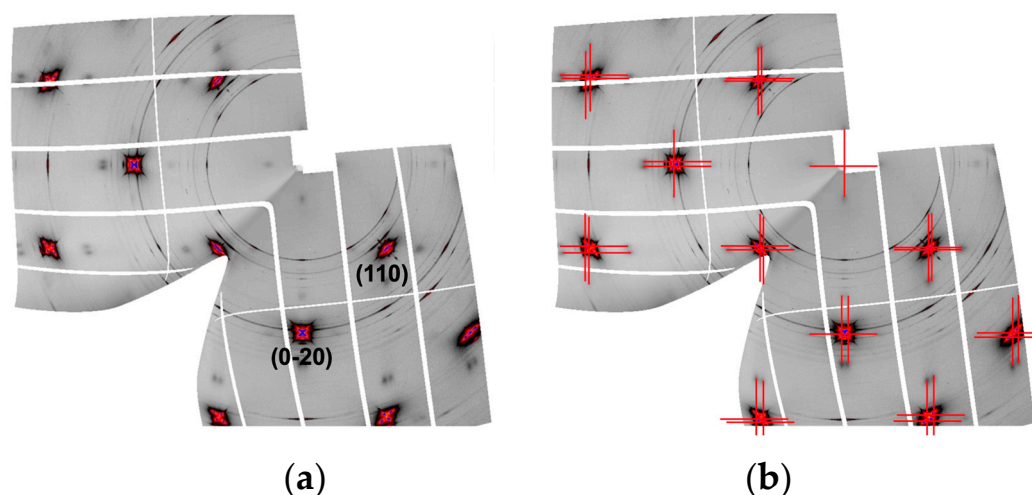
Figure 8. (**a**) Reconstructed (*hk0*)-plane of the reduced $Nd_{1.3}Sr_{0.7}NiO_{3.54}$ crystal, showing beside the basic (*hk0*)-reflections diffuse satellites, which can be indexed applying a unidirectional modulation vector $\mathbf{Q_n} = \pm 0.40\ \mathbf{b^*}$ for all four twin domains (*n*), respectively, for each Bragg reflection $G = ha^* + kb^* + lc^* + mQ$, while $\mathbf{m}$ is limited here to 1st order satellite reflections only. The charge ordering reflections are schematically indicated by red lines in (**b**) and follow in direction of the twin scheme as indicated in Figure 6c. Note that for different twin domains orientations, the modulation vector points into different directions, respectively.

A more complex domain formation is also indicated by the diffuse scattering as shown for the (−*301*) reflection in Figure 7d. This is similar to what has been observed during the electrochemical reduction of $Pr_2NiO_{4+\delta}$ performed at room temperature [32].

Investigations to explore possible oxygen ordering have been carried out by single-crystal synchrotron diffraction at ID28@ESRF, as shown in Figures 7 and 8.

While no extra typical superstructure reflections related to oxygen ordering could be uncovered [33], several broader reflections and powder lines are observed, indicating a partial decomposition into the respective binary oxides, i.e., NiO, Nd_2O_3 and SrO (see Figure A1). We underline that the quantity of the decomposed fraction remains very low and essentially requires synchrotron radiation for its detection, as we were unable to confirm these phases with laboratory diffraction methods (less than 0.2%).

The high brilliance of the synchrotron radiation thus enabled us to highlight slightly broadened reflections, appearing for all main reflections. They can be indexed by a modulation vector $\mathbf{Q_n} = \pm 0.40\ \mathbf{b^*}$, in line with the twin scheme shown in Figure 6c, suggesting a unidirectional Ni^{1+}/Ni^{2+} charge ordering along [010] (see Figure 8b). This value is in between the 1/3 stripe and 1/2 chequerboard like charge ordering as have been reported for Ni^{2+}/Ni^{3+} type nickelates, and is theorized in [34]. The charge ordering is thus along the Ni-O vacancy direction, and consequently, it induces a kind of structural disorder, due to the random distribution of the vacancies, related to the non-stoichiometry. The charge ordering is established as an "average" ordering, rather than a discrete ordering scheme, the latter allowing us to establish rational multiples of the unit cell. A rather arbitrary arrangement as encountered here is also supposed to impact the slightly different Ni^{1+}-O and Ni^{2+}-O bond length distribution on a local scale. It presents thus a valence state ordering, realized on a shorter length scale, which appears by diffraction in an averaged Ni^{1+}-O and Ni^{2+}-O bond length distribution. Despite the random distribution of oxygen vacancies, the charge ordering is of 3D character, as indicated by the presence of respective satellite reflections in higher-order planes, e.g., the (*hk1*)-plane shown in Figure 7d.

4. Conclusions

High-quality single crystals of $Nd_{1.3}Sr_{0.7}NiO_{4+\delta}$ were synthesized by the floating zone method and reduced towards $Nd_{1.3}Sr_{0.7}NiO_{3.54}$ by annealing in a H_2 atmosphere. Despite their high orthorhombicity, they maintained their crystalline integrity throughout the reduction reaction.

The high brilliance of the synchrotron radiation thus enabled us to highlight slightly broadened reflections, appearing for all main reflections. They can be indexed by a modulation vector $\mathbf{Q_n} = \pm 0.4\,\mathbf{b^*}$, suggesting unidirectional Ni^{1+}/Ni^{2+} charge ordering along [010] (see Figure 8). This value is in between the 1/3 stripe and 1/2 chequerboard-like charge ordering as has been reported for Ni^{2+}/Ni^{3+} type nickelates [34]. It thereby appears unusual to observe Ni^{1+}/Ni^{2+} charge ordering already at room temperature, as this kind of electronic ordering is supposed to appear at much lower temperatures, e.g., as found below 100 K for $(Pr_{0.3}La_{0.7})_4Ni_3O_8$ [34]. This might be a consequence of the fixed arrangements of the O-vacancies, favoring to establish charge ordering on a local level. The charge ordering is, however, established as an "average" ordering, rather than a discrete ordering scheme, which would involve rational multiples of the unit cell. It presents thus a locally defined valence state ordering, which, from a structural point of view, appears as a random arrangement of Ni^{1+}-O and Ni^{2+}-O bond length distribution.

A rather arbitrary arrangement as encountered here is also supposed to impact the slightly different Ni^{1+}-O and Ni^{2+}-O bond length distribution on a local scale without long-range ordering. It is, however, unclear whether such an averaged charge ordering in nickelates shows a similar competition towards superconductivity as discussed for d-wave superconductors along the Cu-O-Cu bonds in cuprates [35].

In this regard, Tc gets almost suppressed for striped phased $La_{2-x}Ba_xCuO_4$, alongside the coexisting charge and spin ordering. To judge this influence, a more systematic study on the evolution of charge ordering with the Sr-doping, i.e., changes in the Ni^{1+}/Ni^{2+} ratio, is required.

The general possibility to obtain reduced single crystals despite their increased orthorhombicity must be regarded as a milestone to obtain single crystalline nickelate oxides containing Ni^{1+}/Ni^{2+}, opening to access towards anisotropic properties. The Ni^{1+}/Ni^{2+} valence distribution was evidenced as charge ordering, behaving as in the Sr-doped oxides on an average scale, i.e., not established as long-range translational ordering. An average valence distribution might readily allow charge fluctuations on a shallow energy range, providing an attractive way to identify superconductivity descriptors.

Author Contributions: Conceptualization: W.P. and M.C.; validation: C.H., M.C. and W.P.; formal analysis: C.H., M.C. and W.P.; investigation: W.P., M.C., C.H., A.B. and M.M.; resources: C.H., M.C., A.B. and M.M.; writing—original draft preparation: W.P. and M.C.; writing—review and editing, W.P., M.C., A.B., C.H. and M.M.; visualization, C.H., M.C. and W.P.; supervision, W.P. and P.P. All authors have read and agreed to the published version of the manuscript.
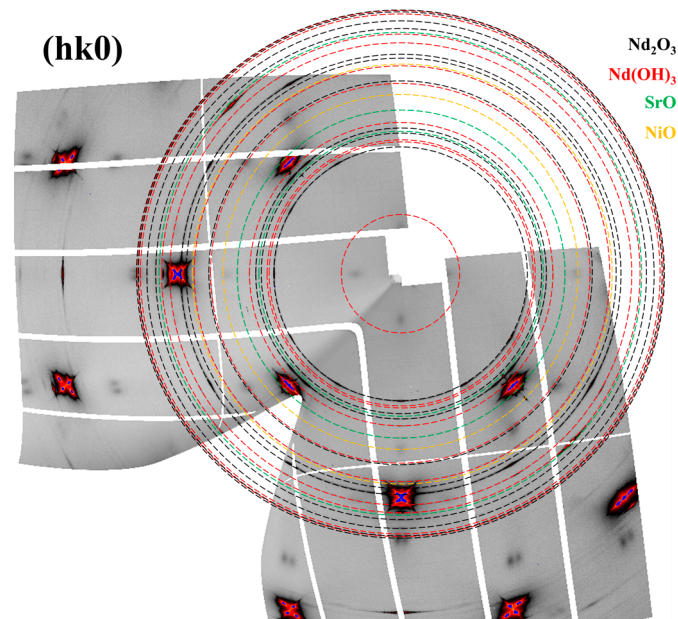
Data Availability Statement: The data presented in this study are available.

Conflicts of Interest: The authors declare no conflict of interest.

Appendix A

Figure A1. Reconstructed (*hk0*)-plane of the reduced $Nd_{1.3}Sr_{0.7}NiO_{3.54}$ single crystals, data obtained on ID28 at ESRF. The observed powder lines indicate a partial decomposition into the respective binary oxides, i.e., NiO, Nd_2O_3 and SrO, simulated by the colored circles.

References

1. Li, D.; Lee, K.; Wang, B.Y.; Osada, M.; Crossley, S.; Lee, H.R.; Cui, Y.; Hikita, Y.; Hwang, H.Y. Superconductivity in an infinite-layer nickelate. *Nature* **2019**, *572*, 624–627. [CrossRef]
2. Anderson, P.W. The Resonating Valence Bond State in La_2CuO_4 and Superconductivity. *Science* **1987**, *235*, 1196–1198. [CrossRef] [PubMed]
3. Spałek, J. Onset of superconductivity, antiferromagnetism, and exchange-mediated pairing in $La_{2−x}Sr_xNiO_4$. *Solid State Commun.* **1989**, *71*, 511–515. [CrossRef]
4. Rao, C.N.R.; Ganguli, A.K.; Nagarajan, R. Superconductivity in layered nickel oxides. *Pramana* **1989**, *32*, L177–L179. [CrossRef]
5. Chow, L.; Yip, K.; Pierre, M.; Zeng, S.; Zhang, Z.; Heil, T.; Deuschle, J.; Nandi, P.; Sudheesh, S.; Lim, Z. Pauli-limit violation in lanthanide infinite-layer nickelate superconductors. *arXiv* **2022**, arXiv:2204.12606. [CrossRef]
6. Chow, L.E.; Sudheesh, S.K.; Luo, Z.; Nandi, P.; Heil, T.; Deuschle, J.; Zeng, S.; Zhang, Z.; Prakash, S.; Du, X. Pairing symmetry in infinite-layer nickelate superconductor. *arXiv* **2022**, arXiv:2201.10038. [CrossRef]
7. Ji, H.; Liu, Y.; Li, Y.; Ding, X.; Xie, Z.; Ji, C.; Qi, S.; Gao, X.; Xu, M.; Gao, P.; et al. Rotational symmetry breaking in superconducting nickelate $Nd_{0.8}Sr_{0.2}NiO_2$ films. *Nat. Commun.* **2023**, *14*, 7155. [CrossRef]
8. Botana, A.S.; Bernardini, F.; Cano, A. Nickelate Superconductors: An Ongoing Dialog between Theory and Experiments. *J. Exp. Theor. Phys.* **2021**, *132*, 618–627. [CrossRef]
9. Harvey, S.P.; Wang, B.Y.; Fowlie, J.; Osada, M.; Lee, K.; Lee, Y.; Li, D.; Hwang, H.Y. Evidence for nodal superconductivity in infinite-layer nickelates. *arXiv* **2022**, arXiv:2201.12971. [CrossRef]
10. Adhikary, P.; Bandyopadhyay, S.; Das, T.; Dasgupta, I.; Saha-Dasgupta, T. Orbital-selective superconductivity in a two-band model of infinite-layer nickelates. *Phys. Rev. B* **2020**, *102*, 100501. [CrossRef]
11. Bandyopadhyay, S.; Adhikary, P.; Das, T.; Dasgupta, I.; Saha-Dasgupta, T. Superconductivity in infinite-layer nickelates: Role of *f* orbitals. *Phys. Rev. B* **2020**, *102*, 220502. [CrossRef]
12. Chen, C.; Ma, R.; Sui, X.; Liang, Y.; Huang, B.; Ma, T. Antiferromagnetic fluctuations and dominant d_{xy}-wave pairing symmetry in nickelate-based superconductors. *Phys. Rev. B* **2022**, *106*, 195112. [CrossRef]
13. Zhou, X.-R.; Feng, Z.-X.; Qin, P.-X.; Yan, H.; Hu, S.; Guo, H.-X.; Wang, X.-N.; Wu, H.-J.; Zhang, X.; Chen, H.-Y.; et al. Absence of superconductivity in $Nd_{0.8}Sr_{0.2}NiO_x$ thin films without chemical reduction. *Rare Met.* **2020**, *39*, 368–374. [CrossRef]
14. Zhang, R.; Lane, C.; Singh, B.; Nokelainen, J.; Barbiellini, B.; Markiewicz, R.S.; Bansil, A.; Sun, J. Magnetic and f-electron effects in $LaNiO_2$ and $NdNiO_2$ nickelates with cuprate-like $3d_{x^2−y^2}$ band. *Commun. Phys.* **2021**, *4*, 118. [CrossRef]
15. Gu, Q.; Li, Y.; Wan, S.; Li, H.; Guo, W.; Yang, H.; Li, Q.; Zhu, X.; Pan, X.; Nie, Y.; et al. Single particle tunneling spectrum of superconducting $Nd_{1−x}Sr_xNiO_2$ thin films. *Nat. Commun.* **2020**, *11*, 6027. [CrossRef] [PubMed]
16. Saxena, A.K. Superconductivity in Cuprates. In *High-Temperature Superconductors*; Springer: Berlin/Heidelberg, Germany, 2012; Volume 125, pp. 129–162.

17. Zeng, S.; Tang, C.S.; Yin, X.; Li, C.; Li, M.; Huang, Z.; Hu, J.; Liu, W.; Omar, G.J.; Jani, H.; et al. Phase Diagram and Superconducting Dome of Infinite-Layer $Nd_{1-x}Sr_xNiO_2$ Thin Films. *Phys. Rev. Lett.* **2020**, *125*, 147003. [CrossRef]

18. Pan, G.A.; Ferenc Segedin, D.; LaBollita, H.; Song, Q.; Nica, E.M.; Goodge, B.H.; Pierce, A.T.; Doyle, S.; Novakov, S.; Córdova Carrizales, D.; et al. Superconductivity in a quintuple-layer square-planar nickelate. *Nat. Mater.* **2022**, *21*, 160–164. [CrossRef]

19. Krockenberger, Y.; Kurian, J.; Winkler, A.; Tsukada, A.; Naito, M.; Alff, L. Superconductivity phase diagrams for the electron-doped cuprates $R_{2-x}Ce_xCuO4$ (R=La, Pr, Nd, Sm, and Eu). *Phys. Rev. B* **2008**, *77*, 060505. [CrossRef]

20. Sun, H.; Huo, M.; Hu, X.; Li, J.; Liu, Z.; Han, Y.; Tang, L.; Mao, Z.; Yang, P.; Wang, B.; et al. Signatures of superconductivity near 80K in a nickelate under high pressure. *Nature* **2023**, *621*, 493–498. [CrossRef]

21. Maity, S.R.; Ceretti, M.; De Barros, R.; Keller, L.; Schefer, J.; Cervellino, A.; Rodríguez Velamazan, J.A.; Paulus, W. Large-scale oxygen order phase transitions and fast ordering kinetics at moderate temperatures in $Nd_2NiO_{4+\delta}$ electrodes. *Mater. Adv.* **2023**, *4*, 651–661. [CrossRef]

22. Maity, S.R.; Ceretti, M.; Keller, L.; Schefer, J.; Meven, M.; Pomjakushina, E.; Paulus, W. Interdependent scaling of long-range oxygen and magnetic ordering in nonstoichiometric $Nd_2NiO_{4.10}$. *Phys. Rev. Mater.* **2021**, *5*, 014401. [CrossRef]

23. De Barros, R.; Ceretti, M.; Schmidt, W.; Pomjakushin, V.Y.; Paulus, W. Growth and Oxygen Stoichiometry Control of High-Quality $La_2CoO_{4+\delta}$ Single Crystals (δ = 0.25). *Cryst. Growth Des.* **2022**, *22*, 5542–5551. [CrossRef]

24. Choisnet, J.; Mouron, P.; Crespin, M.; van Aken, P.A.; Müller, W.F. Perovskite-like intergrowth structure of the reduced cuprate $Nd_2CuO_{3.5}$: A combination of defect and excess oxygen non-stoichiometry phenomena. *J. Mater. Chem.* **1994**, *4*, 895–898. [CrossRef]

25. Houchati, M.I.; Ceretti, M.; Ritter, C.; Paulus, W. From T to T′-La_2CuO_4 via Oxygen Vacancy Ordered $La_2CuO_{3.5}$. *Chem. Mater.* **2012**, *24*, 3811–3815. [CrossRef]

26. Medarde, M.; Rodríguez-Carvajal, J.; Obradors, X.; Vallet-Regi, M.; González-Calbet, J.M.; Sayagués, M.J. Oxygen vacancy ordering in $La_{2-x}Sr_xNiO_{4-\delta}$. *Phys. B Condens. Matter* **1992**, *180–181*, 399–401. [CrossRef]

27. Medarde, M.; Rodríguez-Carvajal, J.; Vallet-Regí, M.; González-Calbet, J.M.; Alonso, J. Crystal structure and microstructure of $Nd_{1.8}Sr_{0.2}NiO_{3.72}$: A K_2NiF_4-type nickelate with monoclinic symmetry and ordered oxygen vacancies. *Phys. Rev. B* **1994**, *49*, 8591–8599. [CrossRef]

28. Wahyudi, O.; Ceretti, M.; Weill, I.; Cousson, A.; Weill, F.; Meven, M.; Guerre, M.; Villesuzanne, A.; Bassat, J.-M.; Paulus, W. Growth of high quality single crystals of strontium doped (Nd,Pr)-nickelates, $Nd_{2-x}Sr_xNiO_{4+\delta}$ and $Pr_{2-x}Sr_xNiO_{4+\delta}$. *CrystEngComm* **2015**, *17*, 6278–6285. [CrossRef]

29. Rodríguez-Carvajal, J. Recent developments of the program FullProf. Commission for Powder Diffraction. *IUCr Newsl.* **2001**, *26*, 12–19. Available online: http://www.ill.eu/sites/fullprof/index.html (accessed on 10 November 2023).

30. Momma, K.; Izumi, F. VESTA 3 for three-dimensional visualization of crystal, volumetric and morphology data. *J. Appl. Crystallogr.* **2011**, *44*, 1272–1276. [CrossRef]

31. Dyadkin, V.; Pattison, P.; Dmitriev, V.; Chernyshov, D. A new multipurpose diffractometer PILATUS@SNBL. *J. Synchrotron Radiat.* **2016**, *23*, 825–829. [CrossRef]

32. Maity, A.; Dutta, R.; Sendtskyi, O.; Ceretti, M.; Lebranchu, A.; Chernyshov, D.; Bosak, A.; Paulus, W. Exploring Fast Room Temperature Oxygen Diffusion in $Pr_2NiO_{4+\delta}$ Stand-Alone Single-Crystalline Electrodes. *Chem. Mater.* **2022**, *34*, 414–421. [CrossRef]

33. Dutta, R.; Maity, A.; Marsicano, A.; Ceretti, M.; Chernyshov, D.; Bosak, A.; Villesuzanne, A.; Roth, G.; Perversi, G.; Paulus, W. Long-range oxygen ordering linked to topotactic oxygen release in $Pr_2NiO_{4+\delta}$ fuel cell cathode material. *J. Mater. Chem. A* **2020**, *8*, 13987–13995. [CrossRef]

34. Chen, X.; Zheng, H.; Phelan, D.P.; Zheng, H.; Lapidus, S.H.; Krogstad, M.J.; Osborn, R.; Rosenkranz, S.; Mitchell, J.F. Competing Charge/Spin-Stripe and Correlated Metal Phases in Trilayer Nickelates $(Pr_{1-x}La_x)_4Ni_3O_8$. *Chem. Mater.* **2022**, *34*, 4560–4567. [CrossRef]

35. Hücker, M.V.; Zimmermann, M.; Gu, G.D.; Xu, Z.J.; Wen, J.S.; Xu, G.; Kang, H.J.; Zheludev, A.; Tranquada, J.M. Stripe order in superconducting $La_{2-x}Ba_xCuO_4$ ($0.095 \leq x \leq 0.155$). *Phys. Rev. B* **2011**, *83*, 104506. [CrossRef]